

Multi-scale stabilization of high-voltage LiCoO₂ enabled by nanoscale solid electrolyte coating



Zeyuan Li^{a,1}, Aijun Li^{a,b,1}, Hanrui Zhang^a, Fanghua Ning^c, Wenxi Li^a, Amirali Zangiabadi^a, Qian Cheng^a, James Joseph Borovilas^a, Yijun Chen^a, Haijun Zhang^{d,*}, Xianghui Xiao^e, Chuying Ouyang^f, Xiaojing Huang^e, Wah-Keat Lee^e, Mingyuan Ge^e, Yong S. Chu^e, Xiuyun Chuan^b, Yuan Yang^{a,**}

^a Program of Materials Science and Engineering, Department of Applied Physics and Applied Mathematics, Columbia University, New York, NY, 10027, United States

^b Key Laboratory of Orogenic Belts and Crustal Evolution, School of Earth and Space Sciences, Peking University, Beijing, 100871, China

^c Department of Energy and Resources Engineering, College of Engineering, Peking University, Beijing, 100871, China

^d Beijing Innovation Center for Materials Genome Engineering, University of Science and Technology Beijing, 10083, China

^e Brookhaven National Laboratory, Upton, NY, 11973, United States

^f Department of Physics, Jiangxi Normal University, Nanchang, 330022, China

ARTICLE INFO

Keywords:

Lithium battery

High voltage

Energy density

LiCoO₂

Li_{1.5}Al_{0.5}Ge_{1.5}(PO₄)₃ nanoparticles

ABSTRACT

LiCoO₂ (LCO) possess a high theoretical specific capacity of 274 mAh g⁻¹, and currently LCO charged to 4.48 V with a capacity of ~190–195 mAh g⁻¹ is penetrating the commercial markets. Scalable strategies to further enhance the performance of LCO are highly attractive. Here, we develop a scalable ball-milling and sintering method to tackle this long-standing challenge by modifying LCO surface with only 1.5–3.5% ceramic solid electrolyte nanoparticles, specifically Li_{1.5}Al_{0.5}Ge_{1.5}(PO₄)₃ (LAGP) as an example. Consequently, the atomic-to-meso multiscale structural stabilities have been significantly improved, even with a high cut-off voltage of 4.5 V vs. Li/Li⁺, leading to excellent electrochemical stabilities. The nano-LAGP modified Li|LCO cell exhibits high discharge capacity of 196 mAh g⁻¹ at 0.1 C, capacity retention of 88% over 400 cycles, and remarkably enhanced rate capability (163 mAh g⁻¹ at 6 C). These results show significant improvement compared to the Li|LCO cells. The as-prepared graphite|LAGP-LCO full cells also show steady cycling with 80.4% capacity retention after 200 cycles with a voltage cut-off of 4.45 V. This work provides a simple and scalable approach to achieve stable cycling of LCO at high voltage with high energy density.

1. Introduction

Lithium-ion batteries (LIBs) have dominated the market of consumer electronics, such as cell phones and laptops, since their first commercialization in 1991 [1,2]. Recently they have been actively developed for electric vehicles and grid-scale energy storage. These rapidly developing markets demand better batteries with both high energy density and long cycle life [3–8]. Among different components in batteries, the cathode capacity is a major limiting factor for energy density since its value (~140–200 mAh g⁻¹) is much less than the anode (e.g. 372 for graphite and 4200 mAh g⁻¹ for silicon) [9–11].

Among various cathode materials, LCO possesses a share of ~31% in

the LIB market, since its well-ordered layered structure enables facile fast and reversible lithium intercalation [12]. LCO has a high theoretical specific capacity of 274 mAh g⁻¹. Conventionally it is thought that the practical discharge capacity is only slightly more than half of the theoretical capacity, ~140 mAh g⁻¹ (Li_{1-x}CoO₂, x ~ 0.5, up to ~4.2 V vs. Li/Li⁺). Such limited capacity originates from two main factors: harmful phase transition in LCO and unstable electrode/electrolyte interface [13–15]. First, when x reaches 0.5 (~4.2 V), the LCO experiences an order–disorder transition from the hexagonal structure (O3 phase) to a monoclinic structure (C2/m phase). When x reaches 0.3 (~4.5 V), another phase transition from O3 to H1-3 occurs [16]. These phase transitions deteriorate electrochemical performance. For example, the

** Corresponding author.

* Corresponding author.

E-mail addresses: zhanghj18@hotmail.com (H. Zhang), yy2664@columbia.edu (Y. Yang).

¹ Zeyuan and Aijun contributed equally to this work.

order–disorder transition substantially lowers the Li^+ diffusivity, and the transition from O3 to H1-3 phase severely stresses the structure, inducing internal strains and micro-cracks within the particles [17]. The second challenge is the instability at the electrode/electrolyte interface. Specifically, Co^{4+} ions are prone to dissolve in the electrolyte at high voltage, which accelerates the electrolyte decomposition and leads to undesired interfacial side reactions [18,19]. All factors mentioned above degrade the electrochemical performance of LCO at high voltage, impeding its practical application in high-energy-density lithium-based batteries.

To improve the cycling stability at high voltage, various strategies have been explored to modify LCO, including heat treatment [20], elemental doping (e.g. Mg [21], Zr [22], Ti [23]), and surface coating (e.g. metal oxide [24], polymers [25]). Solid electrolyte coating has been explored too. Kobayashi applied LAGP coating, but the capacity decreases rapidly from 186 to 105 mAh g^{-1} in the voltage of 3.0–4.4 V at C/8 (0.1 mA cm^{-2}) [26]. Currently LCO charged to 4.48 V with capacity of ~190–195 mAh g^{-1} is penetrating commercial markets.

To push to higher voltage, recently La–Al co-doping was applied to suppress the phase transition during cycling at cut-off voltage of 4.5 V vs. Li/Li^+ , however, only 50 cycles was reported with a capacity retention of 96% [27]. Morimoto et al. applied LAMP coating, and the capacity retention is 89% after 50 cycles between 3.0 and 4.5 V [28]. Ti–Mg–Al co-doping was also employed to suppress the phase transition and promote the cycling stability up to 4.6 V vs. Li/Li^+ [29]. Moreover, Li–Al–F modified LCO was reported to improve the cycling stability at 4.6 V vs. Li/Li^+ [12], but the multi-step hydrothermal preparing process may not be convenient for mass production.

In addition to the modification of cathode materials, electrolytes engineering can also enhance cycle life. The lithium bis-(trifluoromethanesulfonyl) imide (LiTFSI) + lithium bis-(oxalato) borate (LiBOB) + lithium hexafluorophosphate (LiPF_6) tri-salt in carbonate electrolytes, which was first introduced in lithium metal batteries by Zheng et al., could lead to a robust and conductive solid electrolyte interphase [30]. The Li|NCM442 cell with the tri-salt in carbonate electrolyte showed capacity retention as 97.1% after 500 cycles under a high current density of 1.75 mA cm^{-2} between 2.7 and 4.3 V.

In order to be compatible with the potential scalable production, we developed a simple and scalable ball milling and sintering process to modify LCO with trace amount of $\text{Li}_{1.5}\text{Al}_{0.5}\text{Ge}_{1.5}(\text{PO}_4)_3$ (LAGP) (1.5–3.5 wt%) nanoparticles. With the protection of nano-LAGP, the structural and cycling stabilities of LCO have been significantly improved in conventional LiPF_6 -based carbonate electrolyte, even with a high cut-off voltage of 4.5 V vs. Li/Li^+ . Just a trace amount of nano-LAGP endows an impressively high capacity of 196 mAh g^{-1} at 0.1 C, and capacity retention of 88% over 400 cycles at 1 C discharge. Excellent rate capability (163 mAh g^{-1} at 6 C) is also achieved in Li|LAGP-LCO cells. By utilizing an electrolyte with low flammability, 0.6 M lithium bis-(trifluoromethanesulfonyl) imide (LiTFSI) + 0.4 M lithium bis-(oxalato) borate (LiBOB) + 0.05 M LiPF_6 in ethylene carbonate (EC)/propylene carbonate (PC) (EC: PC = 3: 7, v/v) [31], the Li|LAGP-LCO cell delivers steady capacity over 1000 cycles with a capacity retention of 81.0%. Moreover, graphite/LAGP-LCO full cells with N/P ratio of 1.1–1.2 are also demonstrated with a high capacity retention of 80.4%/200 cycles in the range of 2.5–4.45 V. These results are significantly better than their bare LCO counterpart. This work offers an effective method to realize stable and high voltage operation of LCO for high-energy-density rechargeable lithium batteries.

2. Experimental

Synthesis of nano-LAGP modified LCO powder. LiCoO_2 (LCO) and $\text{Li}_{1.5}\text{Al}_{0.5}\text{Ge}_{1.5}(\text{PO}_4)_3$ (LAGP) powder were purchased from MTI Corporation and used as received. The nano-LAGP modified LCO powder was prepared in a scalable and facile method, in which different weight percentage of nano-LAGP (0.5–10%) was ball-milled with LCO powder in isopropanol. The composite was then dried at 80 °C for 6 h and sintered

at 650 °C for 4 h with temperature-increasing and temperature-decreasing rates of both 2.5 °C min^{-1} . The obtained sample was denoted as y% LAGP-LCO, where y represents the ratio of nano-LAGP. The LCO was also sintered under the same condition for comparison.

Preparation of electrolytes. Commercial electrolytes, 1 M LiPF_6 in EC/DEC (EC: DEC = 1: 1, w/w) and 1.2 M LiPF_6 in EC/EMC (EC: EMC = 3: 7, v/v) were kindly provided by Gotion Inc. EC, DEC and EMC are short for ethylene carbonate, diethyl carbonate and ethyl methyl carbonate, respectively. The tri-salt electrolyte was prepared by mixing 0.6 M LiTFSI (Gotion Inc.), 0.4 M LiBOB (Gotion Inc.) and 0.05 M LiPF_6 (Gotion Inc.) in EC (Sigma-Aldrich, 99%)/PC (Sigma Aldrich, 99.7%), where EC/PC were mixed with 7: 3 by volume. For the electrolyte used in graphite|LCO full cells, 1.5 wt% vinylene carbonate (VC, Gotion Inc.) was added in 1.2 M LiPF_6 in EC/EMC (EC: EMC = 3: 7, v/v).

Material Characterizations. Inductively coupled plasma mass spectrometry (ICP-MS) test of samples were tested by Robertson Microлит Laboratories using PerkinElmer Nexlon 300D. X-Ray diffraction (XRD) patterns of the samples were tested by a PANalytical XPert3 Powder XRD with $\text{Cu K}\alpha$ radiation run at 45 mA and 40 V. Two-dimensional (2D) X-ray fluorescence (XRF) elemental imaging was collected by X-ray Fluorescence Microprobe at FXI (8-BM) in the National Synchrotron Light Source II. Scanning electron microscopy (SEM) was characterized on SIGMA VP Zeiss equipped with energy dispersion spectrum (EDS) at 15.0 kV. To unveil the morphology of cycled LCO and LAGP-LCO cathodes, they were washed with pure EC/DEC three times to eliminate electrolyte residue, and then fully dried under vacuum before SEM testing. Transmission electron microscopy (TEM) images of LAGP-LCO particle was conducted on FEI TALOS F200X. X-ray absorption near edge spectroscopy (XANES) [32] was measured at FXI (18-ID) beamline in the National Synchrotron Light Source II. The full-field two-dimensional (2D) XANES with 30 nm spatial resolution across Co K-edge was conducted with TXM.

Battery Assembly. The cathodes were prepared by mixing LAGP-LCO or bare LCO powder, SUPER C65 conductive carbon (Timcal) and poly (vinylidene fluoride) (Kynar 761, Arkema) with a mass ratio of 85:8:7 in N-methyl-2-pyrrolidone (99%, Sigma Aldrich). The mixture was then stirred for 12 h to form a homogeneous slurry and coated on an aluminum foil, followed by drying overnight at 110 °C and cutting into cathodes with a diameter of 15 mm. The graphite anode was prepared by mixing natural graphite (MSE Supplies LLC.), SUPER C65 conductive carbon and poly (vinylidene fluoride) with a mass ratio of 92:3:5 in N-methyl-2-pyrrolidone, then followed the steps of making cathode but the anode was coated on a copper foil and punched into electrode with a diameter of 16 mm. CR2032-type coin cells were assembled in both Li|LCO, Li|LAGP-LCO half cells and graphite|LCO, graphite|LAGP-LCO full cells. The half cells were constructed with bare LCO or LAGP-LCO electrode (active material ~9 mg cm^{-2}), lithium metal anode chip (250 μm thick, 1.56 cm diameter), one piece of polyethylene (PE) separator (Celgard 2325, 25 μm) and liquid electrolytes. The full cells were assembled with bare LCO or LAGP-LCO cathode, natural graphite anode, one piece of PE separator (Celgard 2325, 25 μm), and 1.2 M LiPF_6 in EC/EMC with 1.5 wt% VC as additive. The N/P ratio of full cells was fixed to 1.1–1.2. All of the cells were assembled in an argon-filled glove box with moisture and oxygen levels below 0.1 and 1 ppm, respectively.

Electrochemical Measurements. The cycling performance and rate capability of half cells and full cells were conducted on Wuhan LAND battery testers. The cells were carried out with constant current and constant voltage mode, when the cells reached the charge cut-off voltage, a constant voltage charge process was applied until current decreased to 0.05 C. Charge and discharge current rates of 0.3–6 C were utilized to investigate the power rate of cathodes with different electrolytes. Electrochemical impedance spectroscopy (EIS) was measured on a VMP3 multichannel potentiostat from Bio-Logic in a frequency range of 1 MHz to 0.1 Hz with a 10 mV amplitude. All of the cells were tested at room temperature.

DFT calculation details. All the quantum mechanical calculations based on density functional theory (DFT) were implemented in the

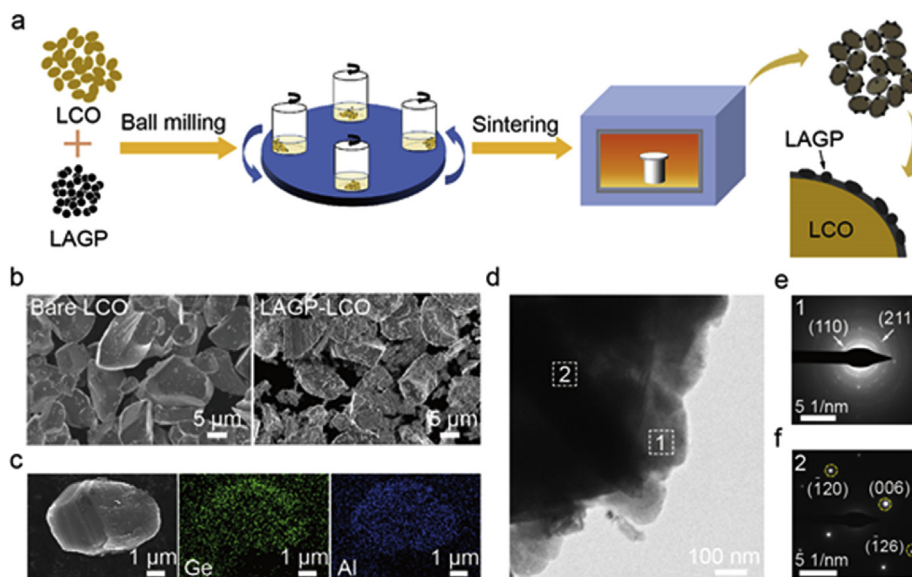


Fig. 1. Synthesis and characterizations of LAGP-LCO particles. (a) The preparation process to modify LCO particle by nano-LAGP. (b) SEM images of bare LCO and LAGP-LCO particles. (c) EDS maps of Co, Ge and Al in LAGP-LCO particle. (d) A TEM image of an as-prepared LAGP-LCO particle. (e, f) Diffraction patterns of (e) LAGP and (f) bulk LCO, which correspond to region 1 and 2 in (d), respectively.

Vienna ab initio Simulation Package (VASP 5.4.4) [33]. The projector augmented wave (PAW) method [34] with a kinetic energy cutoff of 520 eV is employed. The spin-polarized generalized gradient approximation (GGA) with PBE function [35] was used to treat the electron exchange–correlation interactions. The GGA + U method was used with a U values of 4.91 eV for Co 3d states, according to Ref. [36]. Furthermore, we considered the van der Waals interaction throughout the calculations. The Monkhorst–Pack scheme [37], with a $2 \times 3 \times 1$ k-point mesh, was used for the integration in the irreducible Brillouin zone. The lattice parameters and ionic position were fully relaxed, and the final forces on all atoms were less than $0.01 \text{ eV } \text{Å}^{-1}$. Density of states calculations were

smearing using the Gaussian smearing method with a smearing width of 0.05 eV. The LiCoO_2 (104) surface was simulated using the symmetric periodic slab model containing 42 Li atoms, 84 O atoms and 42 Co atoms, with consecutive slabs separated by an 18 Å vacuum layer. The Ge modified slab systems were modelled by substituting 1 out of 42 Co ions with a Ge ion.

3. Results and discussion

Synthesis and Characterizations of LAGP-modified LCO cathode.

Nano-LAGP modification was realized by a scalable and facile ball

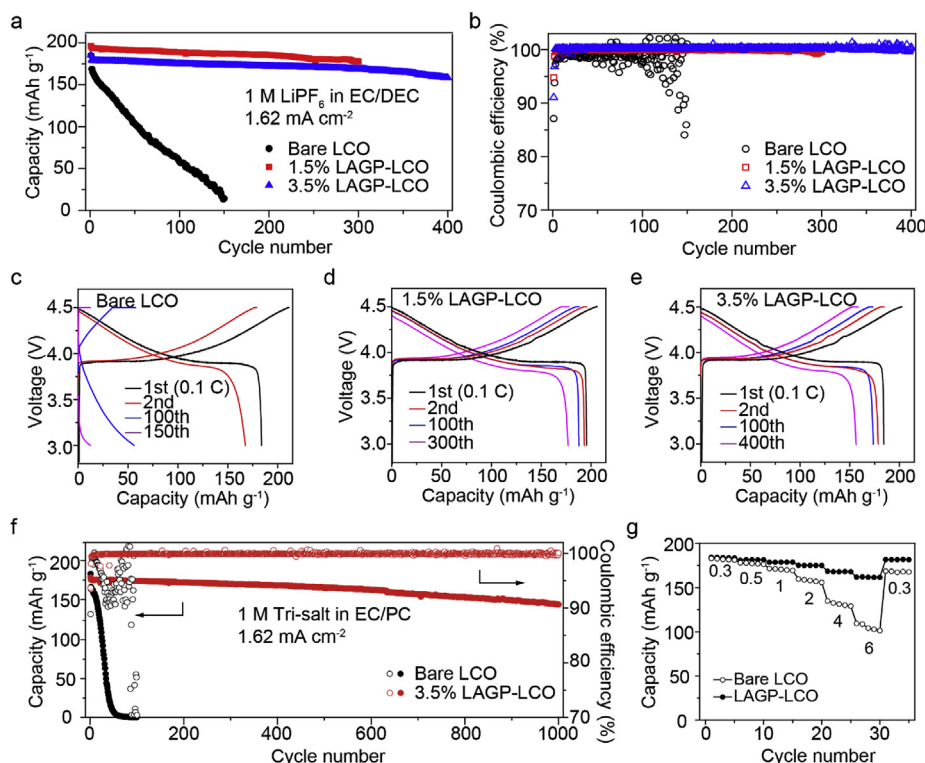


Fig. 2. Electrochemical performance of Li|LCO and Li|LAGP-LCO cells in the voltage range of 3.0–4.5 V. (a) Discharge capacity and (b) Coulombic efficiency vs. cycle number with 1 M LiPF_6 in EC/DEC (EC: DEC = 1: 1, w/w). (c–e) voltage profiles of (c) Li|LCO, (d) 1.5 wt% Li|LAGP-LCO and (e) 3.5 wt% Li|LAGP-LCO cells. (f) Cycling performance of 3.5 wt% Li|LAGP-LCO cell and Li|LCO cell with tri-salt electrolyte (0.6 M $\text{LiTFSI} + 0.4 \text{ M LiBOB} + 0.05 \text{ M LiPF}_6$ in EC/PC (EC: PC = 3: 7, v/v)). All these cells were charged at 0.49 mA cm^{-2} (0.3 C) and discharged at 1.62 mA cm^{-2} (1 C), before which the cells were pre-cycled at 0.1 C for one cycle. (g) Rate performance of 3.5 wt% Li|LAGP-LCO and Li|LCO cells with 1 M LiPF_6 in EC/DEC. The charging and discharging currents are the same for each C-rate.

milling and sintering process, as shown in Fig. 1a. First, LiCoO₂ particles were ball milled with different amount of LAGP nanoparticles (0.5–10 wt %) at a grinding speed of 750 rpm in isopropanol. The mixture was then dried at 80 °C for 6 h and sintered at 650 °C for 4 h to obtain nano-LAGP modified LCO powders. After the modification, no structural change was observed in X-ray diffraction (XRD) (Fig. S1), indicating the perseverance of the LCO structure. Scanning electron microscopy (SEM) shows that the surface of LCO becomes rough and is decorated with LAGP nanoparticles (Fig. 1b). Two-dimensional (2D) X-ray fluorescence (XRF) chemical map display a nearly conformal Ge signal on Co (Fig. S2). EDS mapping equipped with SEM also unveils that Ge and Al signals cover the entire particle with nearly uniform distribution (Fig. 1c and Fig. S3). Based on XRF and EDS imaging, we estimate that 80–90% of surface is covered by LAGP. Although 10–20% is still exposed, such reduced exposure can reduce electrolyte oxidation. Moreover, we suspect that Al and Ge can diffuse around to exposed surface, which help passivate the interface and will be discussed below.

The existence of LAGP is further verified by transmission electron microscopy (TEM) (Fig. 1d). For example, the electron diffraction pattern (DP) of region 1 displays rings which match well with the (110) and (211) planes of LAGP (Fig. 1e, JCPDS No. 80–1924). The DP of region 2 shows spots corresponding to ($\bar{1}$ 20), (006) and ($\bar{1}$ 26) planes in layered LCO (R-3m space group) (Fig. 1f). All characterizations above indicate the modification of LCO by LAGP nanoparticles has been successfully realized by this simple and scalable process without changing the crystal structure of LCO. At lab scale, dry ball milling is difficult to achieve ultrahigh uniformity compared to sol-gel method. However, as it is widely used in industry for its low cost and efficiency, we expect better homogeneity to be achieved at larger scale after more optimization.

Electrochemical performance of Li|LCO half cells. To evaluate how the nano-LAGP modification enhances the electrochemical stability of LCO, the as-prepared LAGP-LCO cathode was first tested in Li|LAGP-LCO half cells with commercial carbonate electrolytes. All LCO electrodes have a capacity of ~ 1.6 mAh cm⁻², and the cells are cycled between 3 and 4.5 V. Inductively coupled plasma mass spectrometry (ICP-MS) shows that the actual content of LAGP is 4.7 wt% for the nominal 3.5% LAGP-LCO sample, and other samples also show slightly higher actual content than the nominal value. In following paragraphs, the specific capacities have been corrected based on actual content.

As shown in Fig. 2a, when commercial electrolyte, 1 M LiPF₆ in EC/DEC is used, bare LCO shows an initial discharge capacity of 184 mAh g⁻¹ at 0.1 C, and the capacity drops fast from 168 to 54.3 mAh g⁻¹ within 100 cycles at 0.3 C charging and 1 C discharging. After LCO is modified with 1.5 wt% and 3.5 wt% LAGP, the initial discharge capacity at 0.1 C remain at 196 and 185 mAh g⁻¹, respectively. Moreover, the capacity retention significantly enhances to 91.8%/300 cycles (194–178 mAh g⁻¹) for 1.5 wt% nano-LAGP, and 88.3%/400 cycles (179–158 mAh g⁻¹), for 3.5 wt% nano-LAGP respectively. On the other side, nano-LAGP coating also reduces interfacial side reaction, as reflected by higher and more stable CE (Fig. 2b). Meanwhile, the voltage hysteresis of Li|LCO cell increases quickly from 0.04 to 1 V within 150 cycles (Fig. 2c), while the voltage hysteresis is quite steady for Li|LAGP-LCO cells. It only increases slightly from 0.04 to 0.09 V after 300 cycles for 1.5 wt% LAGP (Fig. 2d), and from 0.05 to 0.09 V after 400 cycles for 3.5 wt% LAGP (Fig. 2e). These results no doubt show that LAGP nano-coating can significantly enhance the cycling performance of LCO. More cycling results with different nano-LAGP percentages and another carbonate electrolyte (1.2 M LiPF₆ in EC/EMC) are illustrated in Figs. S4 and S5, showing the versatility of this approach.

In addition, the nano-LAGP percentage is surveyed from 0 to 10 wt% to better understand its effect on the performance of LCO (Fig. S6). When the nano-LAGP percentage increases from 0 to 10% in 1 M LiPF₆ in EC/DEC electrolyte, the initial specific capacity first increases slightly from 184 mAh/g at 0 wt% to 196 mAh/g at 1.5 wt%, and gradually decreases to 165 mAh/g at 10 wt% (Fig. S6). Meanwhile, the capacity retention

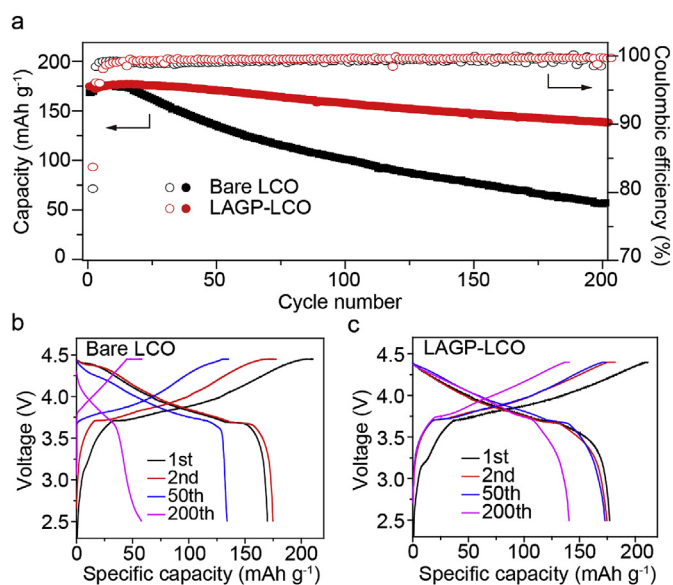


Fig. 3. Electrochemical performance of full cells based on LCO and nature graphite. (a) Cycling performance of full-cells with 3.5% LAGP-LCO and bare LCO cathodes at room temperature in the voltage range of 2.5–4.45 V. The current density is 0.32 mA cm⁻² (0.2 C). (b–c) Voltage profiles of full-cells with (b) bare LCO and (c) 3.5% LAGP-LCO electrodes.

sharply increases from 33.6%/100 cycles at 0 wt% to 97.2%/100 cycles at 1.5 wt%, and keeps at a nearly constant value with further increase of capacity retention. Similar trend is also observed in other carbonate electrolytes (Fig. S4).

The cycling performance can be further improved by using electrolytes that can form a passivation layer on the cathode surface through salt decomposition [30]. For example, when the tri-salt electrolyte (0.6 M LiTFSI + 0.4 M LiBOB + 0.05 M LiPF₆ in EC/PC (EC: PC = 3: 7, v/v)) is used together with LAGP nano-coating, an ultra-stable cycling is achieved with a capacity retention of 82.1% over 1000 cycles (Fig. 2f). Conversely, bare LCO even cannot endure 100 cycles with almost no capacity remained. It is worth noticing that the capacity decay in Li|LAGP-LCO cell is not ascribed to the failure of LCO itself, but to the lithium anode and electrolytes. This is validated by the recovering of capacity when the cycled lithium anode and electrolytes are renewed (Fig. S7). A closer look of cycled lithium chip shows a loose and fragile surface, which may arise from the non-uniform lithium deposition (Fig. S8).

Besides remarkably enhanced cycling stability, nano-LAGP modification also provides better power capability (Fig. 2g). When 3.5 wt% nano-LAGP is applied, the reversible specific capacity reaches 185, 180, 179, 177, 168 and 163 mAh g⁻¹ at 0.3, 0.5, 1, 2, 4 and 6 C with 1 M LiPF₆ in EC/DEC, respectively. In contrast, bare LCO cell only exhibits specific capacity of 183, 178, 171, 159, 133 and 109 mAh g⁻¹ at 0.3, 0.5, 1, 2, 4 and 6 C, respectively, much lower than those with nano-LAGP modification. Similar enhanced power capability is also observed with 1.2 M LiPF₆ in EC/EMC (Fig. S9a) and 1 M tri-salt in EC/PC (Fig. S9b), and corresponding voltage profiles are exhibited in Fig. S10. The improved power capability probably arises from faster interfacial ionic transport and bulk ionic diffusion, especially after several cycles. This is consistent with impedance results in Fig. 5a and Fig. 5b. This will be later discussed in details together with other characterization results.

Electrochemical performance of LCO/graphite full cells. To demonstrate imminent applicability, 3.5% LAGP-LCO is combined with a nature graphite (NG) anode for full cell cycling. The negative/positive (N/P) ratio is 1.1–1.2 and the full cell voltage range is 2.5–4.45 V. 1.2 M LiPF₆ in EC/EMC with 1.5 wt% vinylene carbonate (VC) additive is used. As shown in Fig. 3a, the initial specific capacity of the NG|LAGP-

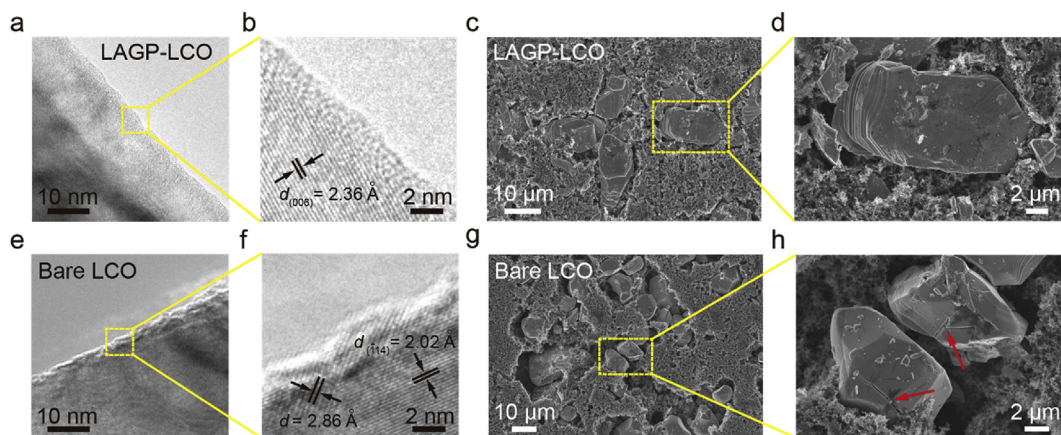


Fig. 4. Characterizations of LAGP-LCO and bare LCO cathodes after 100 cycles. (a–b) High resolution TEM and (c–d) SEM images of cycled LAGP-LCO cathode. (e–f) High resolution TEM and (g–h) SEM images of cycled bare LCO cathode. (b), (d), (f), and (h) are zoom in images of (a), (c), (e) and (g), respectively. The red arrows indicate cracks in bare LCO particles after 100 cycles. (For interpretation of the references to colour in this figure legend, the reader is referred to the Web version of this article.)

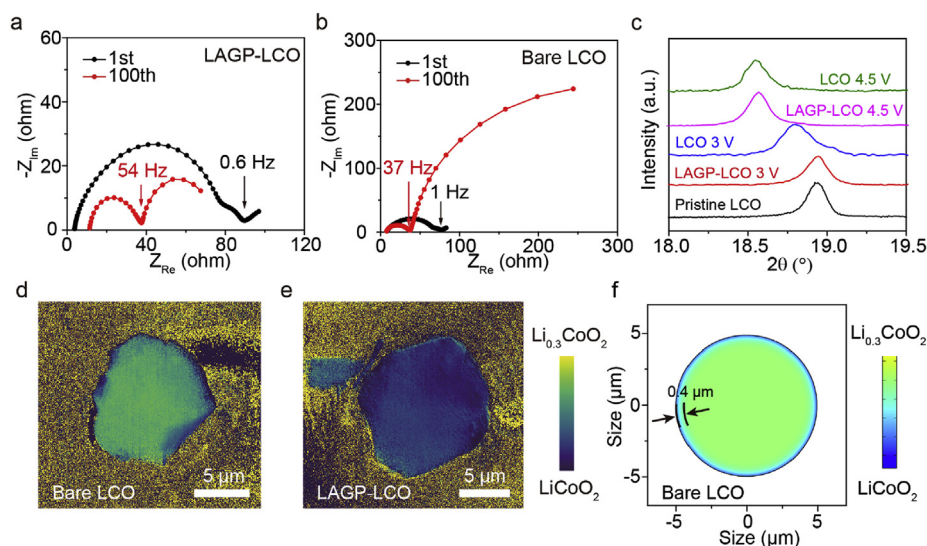


Fig. 5. Characterizations of cycled bare LCO and LAGP-LCO cathodes. (a–b) EIS results of (a) Li|LAGP-LCO and (b) Li|LCO cells between 1 MHz and 0.1 Hz. Both the 1st cycle and the 100th cycle were taken at the charged state (4.5 V vs. Li/Li⁺). (c) XRD of LAGP-LCO and bare LCO after 50 cycles in the charged state (4.5 V) and the discharged state (3 V). (d–e) Representative 2D XANES chemical maps of Co on (d) a bare LCO particle and (e) a 3.5 wt% LAGP-LCO particle after 50 cycles. Both electrodes were imaged at the discharge state (3 V). (f) 2D simulation by COMSOL for lithium concentration in bare LCO cathode after lithiated.

LCO cell is 177 mAh g⁻¹ at 0.1 C, higher than that of NG|LCO cell (170 mAh g⁻¹). The discrepancy with results in Li|LAGP-LCO cell is attributed to un-optimized initial CE of the graphite anode. However, the initial CE of the NG|LAGP-LCO cell (83.7%) is still higher than that of the NG|LCO cell (80.7%). Upon cycling, the specific capacity in NG|LCO cell decays quickly from 170 mAh g⁻¹ to only 58.1 mAh g⁻¹ (34.2% retention) after 200 cycles at 0.2 C (Fig. 3a and b). In contrast, the NG|LAGP-LCO cell shows remarkably improved cycling stability. The specific capacity increases from 175 mAh g⁻¹ to 180 mAh g⁻¹ in the 15th cycle at 0.2C and remains at 141 mAh g⁻¹ (80.6%) after 200 cycles (Fig. 3a and c). In addition, NG|LAGP-LCO cell displays higher average CE of 99.4% than 99.0% in NG|LCO cell.

Moreover, excellent rate capability is also observed in full cell with nano-LAGP modification, featuring reversible capacity of 178, 169, 158, and 144 mAh g⁻¹ at 0.2, 1, 3, and 5 C, respectively. In contrast, the NG|LCO cell only deliver specific capacity of 173, 137, 54.4, and 3.3 mAh g⁻¹ at 0.2, 1, 3, and 5 C without nano-LAGP modification, respectively (Fig. S11). All results above indicate the trace amount of nano-LAGP enables stable cycling performance of LCO in the high-voltage operation.

Mechanistic study of electrochemical stability. To understand

why trace amount of nano-LAGP dramatically enhances electrochemical performance of LCO charged to high voltage, multi-mode characterizations are utilized to unveil structural and chemical transformations in the cathode, including TEM, XRD and full-field transmission X-ray microscopy (TXM) with X-ray absorption near edge structure (XANES), SEM, and electrochemical impedance spectroscopy (EIS).

Electron microscopies first unveil that the LAGP nano-coating well preserves the structural integrity of LCO at both atomic and mesoscales, while atomic re-arrangement and micro-cracks are frequently observed in bare LCO. First, in LAGP-LCO after 100 cycles, clean layered structure is observed at the edge of LAGP-modified LCO (Fig. 4a and b), which indicates well-preserved crystal structures inside. The LAGP nanoparticles on surface remain intact after cycling (Fig. S12). Moreover, no obvious micro cracks are observed in SEM images (Fig. 4c–d and Figs. S13a–b). On the other side, TEM illustrates re-arrangement of atoms at the surface of bare LCO after 100 cycles (Fig. 4e and f). The interplanar spacing of 2.02 Å inside the particle can be ascribed to (114) plane of LCO, however, the interplanar spacing of 2.86 Å does not belong to any spacing in pristine LCO (JCPDS No. 75–0532), indicating the appearance of a new phase. In addition, cracks with length of 0.5–5 μm and width of 20–150 nm are frequently observed in LCO (Fig. 4g and h). More

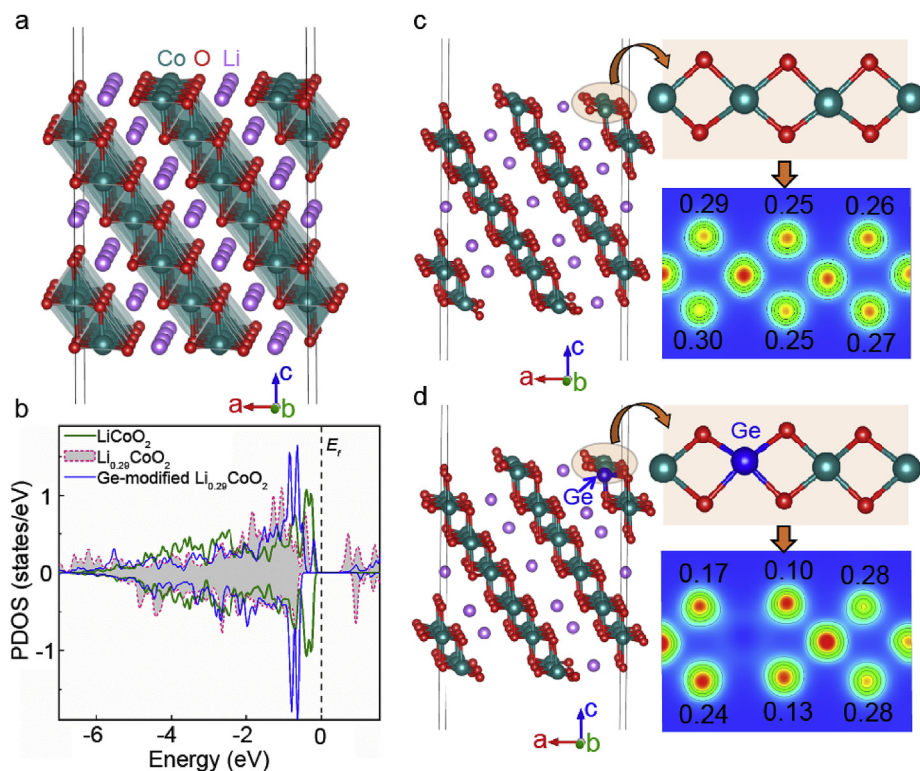


Fig. 6. DFT simulation of LCO and Ge on LCO. (a) Optimized atomic structure of the (104) slab of LiCoO₂. (b) PDOS of surface O ions in LiCoO₂, Li_{0.29}CoO₂ and Ge-modified Li_{0.29}CoO₂ system. The chosen O ions for PDOS in Ge-modified system are around Ge ions. The E_f (Fermi level) is set to be 0 eV. (c–d) Optimized atomic structures of the (104) slab system of (c) Li_{0.29}CoO₂ and (d) Ge-modified Li_{0.29}CoO₂. The insets on the right-hand side of (c) and (d) are the corresponding surface structures (top) and two-dimensional charge density distributions (bottom) displayed in top views. The values beside the charge density contours are the amount of electron loss of the corresponding O ion upon delithiation from LiCoO₂ to Li_{0.29}CoO₂ obtained from Bader charge analysis.

examples can be found in Figs. S13c–d. The cracks not only increase the surface area of bulk LCO which promotes undesired cathode/electrolyte side reactions, but also cause strain and damage in the LCO, leading to deterioration in cycling performance [38,39].

Such enhanced structural integrity across multi-scale leads to stable impedance and reversible ion intercalation in nano-LAGP modified LCO. This is first validated by EIS measurements. In LAGP-LCO, the impedance at 4.5 V even slightly decreases after 100 cycles (Fig. 5a), since the lithium anode typically shows reduced impedance at the beginning of cycling due to increased surface area [40,41]. In contrast, although the electrolyte resistance and charge transfer resistance do not change significantly after 100 cycles in bare LCO at 4.5 V, the diffusion tail becomes much longer after 100 cycles (Fig. 5b). This can be attributed to structural deterioration observed in TEM and SEM (Fig. 4f, h). First, a damaged surface layer of 2–5 nm (e.g. Fig. 4f) is enough to result in obvious change in the so called “bulk” diffusion tail. For example, if the ionic diffusivity is reduced to 10^{-14} cm² s⁻¹ in the damaged surface layer, ions can only move ~3 nm in 10 s (for 0.1 Hz). Hence, the sluggish ion diffusion is reflected as the diffusion tail, as supported by COMSOL simulations (Fig. S14 and supplementary note 1). Second, the micro cracks observed by SEM suggest large strain inside LCO, which can also lead to poorer crystallinity and more sluggish ionic transport inside.

The structural stability and consequent stable impedance lead to more reversible Li⁺ intercalation in nano-LAGP modified LCO, as validated by XRD and TXM studies. The XRD pattern shows that the (003) peak in LAGP-LCO in the discharged state after 50 cycles remain at 18.94° in 2θ (Fig. 5c), which is the same as that in pristine LCO. This indicates that the Li⁺ intercalation is fully reversible. In contrast, the (003) peak in bare LCO after 50 cycles remains at 18.79°, corresponding to ~Li_{0.6}CoO₂. This suggests that Li⁺ is difficult to intercalate inside due to the interfacial structural deterioration observed in TEM, and thus the XRD peak cannot be fully shifted to the discharged state.

The XRD results are also echoed by *ex-situ* 2D TXM XANES images of LCO after 50 cycles, which also unveils heterogeneity in ion intercalation. In bare LCO, when discharged to 3.0 V, only the surface layer is fully lithiated and stays at the LiCoO₂ state, but the bulk remains at ~

Li_{0.5}CoO₂ state (Fig. 5d) and the peak of Co K-edge peak shifts to 7.729 keV (Fig. S15). This is consistent with observations above that the surface of LCO is damaged so that Li⁺ are difficult to diffuse inside. Such core/shell-like distribution is also confirmed by COMSOL simulations (Fig. 5f and supplementary note 1). On the other side, 3.5 wt% LAGP-LCO discharged to 3.0 V shows the correct oxidation state at 7.727 keV (Fig. S15), which corresponds to Co³⁺ (see Fig. S16 for the reference) and validates reversible Li⁺ intercalation inside.

By combining results from multi-mode characterizations above, it can be concluded the nano-LAGP plays an essential role in stabilizing the structure of LCO from atomic to mesoscale, and facilitating interfacial and bulk ion transport, which leads to reversible ion intercalation and thus high power density and excellent cycling performance.

Besides surface coating, it is also expected that Al and Ge can be incorporated into LiCoO₂ lattice due to post-annealing at 650 °C after ball milling, which could also enhance the stability. It should be noted that in TEM we don't see evidence that Al and Ge are indeed incorporated inside, but it may be due to the low concentration (<1%), so that they cannot be detected by EDS. Here the following discussion is based on the assumption that they are in LiCoO₂ lattice, which provides a possible mechanism for stabilization, but requires further confirmation.

While the stabilization effect of Al has been studied [27,42,43], Ge substitution was rarely explored. Hence, density functional theory (DFT) calculations were conducted to study the role of surface-Ge on the surface stability of LiCoO₂ cathode during charge/discharge process. (104) surface of LiCoO₂ is chosen due to its low energy compared to other surfaces (see supplementary note 2 for more discussion). In DFT simulation, it is first found that Ge prefers to stay at surface than the bulk due to lower energy, and thus surface substitution of Ge is used (Fig. S17). As illustrated in Fig. 6b, PDOS (partial density of states) of O ions shows that O-redox occurs during the delithiation process from LiCoO₂ (green line) to Li_{0.29}CoO₂ (shaded dot red line), as reflected by less states below E_f and more states above and close to E_f . Regarding to the effect of Ge doping, the PDOS of surface-O ion near Ge ion in Ge modified Li_{0.29}CoO₂ system (blue line) remains more occupied O-2p states (below E_f) whereas less unoccupied states (above E_f) than that of the surface-O ion in pristine

Li_{0.29}CoO₂ system, which indicates that the charge compensation provided by surface-O ions is mitigated by surface-Ge, and thus O becomes more stable on the surface. The relaxed structures of delithiated state (Li_{0.29}CoO₂) of pristine and modified cases are shown in Fig. 6c and d, respectively. The Bader charge analysis is further conducted to verify the charge compensation provided by surface-O-redox. The amount of electron loss of surface-O ions evaluated by Bader charge analysis is shown on the right-hand side of Fig. 6c and d, which shows that the surface-O ions around the Ge ions lose less charge compared with those without Ge ions nearby. These results are consistent with PDOS of surface-O ions. Hence, we conclude that the surface-O ions around Ge ions hold more charge than pristine one in the delithiated state, as Ge ion on the surface helps to resist the charge deficiency of the surface-O ions, thus stabilized the surface-O ions. This can be another reason why LAGP-LCO exhibits significantly better stability at high electrode potential.

In summary, we have demonstrated that a trace amount of nano-LAGP can well modify the surface of LiCoO₂, and significantly improve the multi-scale structural stability and thus the cycling performance, even at a high cut-off voltage of 4.5 V vs Li/Li⁺. The LAGP nano-coating preserves the layered structure of LCO at the atomic scale and the integrity of the particle at mesoscale, as validated by electron microscopic and Synchrotron-based characterizations. DFT simulation further demonstrates that Ge ions can stabilize Oxygen ions on the surface of LiCoO₂. Hence, the electrochemical impedance is stabilized, leading to remarkably enhanced cycling performance. Li|LAGP-LCO cells exhibit ultrahigh discharge capacity of 194.4 mAh g⁻¹, capacity retention of 88% over 400 cycles, together with remarkably enhanced rate capability (161 mAh g⁻¹ at 6 C). Moreover, NG|LAGP-LCO full cells also show stable cycling with capacity retention of 83.0% after 150 cycles. This work presents a simple and scalable approach to realize stable, high-voltage operation of LCO for lithium batteries with high energy density.

Declaration of competing interest

The authors declare that they have no known competing financial interests or personal relationships that could have appeared to influence the work reported in this paper.

CRediT authorship contribution statement

Zeyuan Li: Conceptualization, Methodology, Formal analysis, Data curation, Writing - original draft, Writing - review & editing. **Aijun Li:** Conceptualization, Methodology, Formal analysis, Investigation, Data curation, Writing - original draft. **Hanrui Zhang:** Methodology, Validation, Conceptualization, Investigation. **Fanghua Ning:** Formal analysis, Resources, Visualization. **Wenxi Li:** Formal analysis, Visualization. **Amirali Zangiabadi:** Formal analysis. **Qian Cheng:** Writing - review & editing. **James Joseph Borovilas:** Writing - review & editing. **Yijun Chen:** Formal analysis. **Haijun Zhang:** Methodology, Supervision, Writing - review & editing. **Xianghui Xiao:** Formal analysis, Resources. **Chuying Ouyang:** Formal analysis, Resources. **Xiaoqing Huang:** Formal analysis, Resources. **Wah-Keat Lee:** Resources. **Mingyuan Ge:** Resources. **Yong S. Chu:** Resources. **Xiuyun Chuan:** Conceptualization, Investigation. **Yuan Yang:** Conceptualization, Methodology, Supervision, Writing - review & editing.

Acknowledgments

Dr. Y. Yang acknowledges support from Research Corporation for Science Advancement under award no. 26293. A. J. Li would like to acknowledge the financial support from the China Scholarship Council (No. 201706010086) and X. Y. Chuan acknowledges the National Natural Science Foundation of China (No. 51774016). This research used resources of the 18-ID (FXI) and 3-ID (HXN) beamline of the National

Synchrotron Light Source II, a U.S. Department of Energy (DOE) Office of Science User Facility operated for the DOE Office of Science by Brookhaven National Laboratory under Contract No. DE-SC0012704.

Appendix A. Supplementary data

Supplementary data to this article can be found online at <https://doi.org/10.1016/j.ensm.2020.03.031>.

References

- [1] S. Xia, X. Wu, Z. Zhang, Y. Cui, W. Liu, *Chem* 5 (2019) 753–785.
- [2] A. Chagnes, J. Swiatowska, *Lithium Process Chemistry: Resources, Extraction, Batteries, and Recycling*, Elsevier, 2015.
- [3] A. Manthiram, X. Yu, S. Wang, *Nat. Rev. Mater.* 2 (2017) 16103.
- [4] B. Dunn, H. Kamath, J.-M. Tarascon, *Science* 334 (2011) 928.
- [5] D. Larcher, J.M. Tarascon, *Nat. Chem.* 7 (2014) 19–29.
- [6] P. Albertus, S. Babinec, S. Litzelman, A. Newman, *Nat. Energy* 3 (2018) 16–21.
- [7] Q. Cheng, A. Li, N. Li, S. Li, A. Zangiabadi, W. Huang, A.C. Li, T. Jin, Q. Song, W. Xu, *Joule* 3 (2019) 1510–1522.
- [8] G. Qian, B. Zhu, X. Liao, H. Zhai, A. Srinivasan, N.J. Fritz, Q. Cheng, M. Ning, B. Qie, Y. Li, *Adv. Mater.* 30 (2018) 1704947.
- [9] D. Deng, *Energy Sci. Eng.* 3 (2015) 385–418.
- [10] R. Chen, R. Luo, Y. Huang, F. Wu, L. Li, *Adv. Sci.* 3 (2016) 1600051.
- [11] C. Liu, Z.G. Neale, G. Cao, *Mater. Today* 19 (2016) 109–123.
- [12] J. Qian, L. Liu, J. Yang, S. Li, X. Wang, H.L. Zhuang, Y. Lu, *Nat. Commun.* 9 (2018) 4918.
- [13] T. Mizokawa, Y. Wakisaka, T. Sudayama, C. Iwai, K. Miyoshi, J. Takeuchi, H. Wadati, D.G. Hawthorn, T.Z. Regier, G.A. Sawatzky, *Phys. Rev. Lett.* 111 (2013), 056404.
- [14] J.N. Reimers, J.R. Dahn, U. von Sacken, *J. Electrochem. Soc.* 140 (1993) 2752–2754.
- [15] J. Kikkawa, S. Terada, A. Gunji, T. Nagai, K. Kurashima, K. Kimoto, *J. Phys. Chem. C* 119 (2015) 15823–15830.
- [16] L. Liu, L. Chen, X. Huang, X.-Q. Yang, W.-S. Yoon, H.S. Lee, J. McBreen, *J. Electrochem. Soc.* 151 (2004) A1344–A1351.
- [17] L. Wang, B. Chen, J. Ma, G. Cui, L. Chen, *Chem. Soc. Rev.* 47 (2018) 6505–6602.
- [18] R.V. Chebiam, A.M. Kannan, F. Prado, A. Manthiram, *Electrochem. Commun.* 3 (2001) 624–627.
- [19] D. Enslin, G. Cherkashinin, S. Schmid, S. Bhuvanewari, A. Thissen, W. Jaegermann, *Chem. Mater.* 26 (2014) 3948–3956.
- [20] Z. Chen, J. Dahn, *Electrochem. Solid State Lett.* 7 (2004) A11–A14.
- [21] H.-S. Kim, T.-K. Ko, B.-K. Na, W.I. Cho, B.W. Chao, *J. Power Sources* 138 (2004) 232–239.
- [22] X. Yang, L. Shen, B. Wu, Z. Zuo, D. Mu, B. Wu, H. Zhou, *J. Alloys Compd.* 639 (2015) 458–464.
- [23] S. Gopukumar, Y. Jeong, K.B. Kim, *Solid State Ionics* 159 (2003) 223–232.
- [24] J.-H. Shim, S. Lee, S.S. Park, *Chem. Mater.* 26 (2014) 2537–2543.
- [25] Z. Yang, R. Li, Z. Deng, *Sci. Rep.* 8 (2018) 863.
- [26] Y. Kobayashi, S. Seki, M. Tabuchi, H. Miyashiro, Y. Mita, T. Iwahori, *J. Electrochem. Soc.* 152 (2005) A1985.
- [27] Q. Liu, X. Su, D. Lei, Y. Qin, J. Wen, F. Guo, Y.A. Wu, Y. Rong, R. Kou, X. Xiao, F. Aguesse, J. Bareño, Y. Ren, W. Lu, Y. Li, *Nat. Energy* 3 (2018) 936–943.
- [28] H. Morimoto, H. Awano, J. Terashima, Y. Shindo, S. Nakanishi, N. Ito, K. Ishikawa, S.-i. Tobishima, *J. Power Sources* 240 (2013) 636–643.
- [29] J.-N. Zhang, Q. Li, C. Ouyang, X. Yu, M. Ge, X. Huang, E. Hu, C. Ma, S. Li, R. Xiao, W. Yang, Y. Chu, Y. Liu, H. Yu, X.-Q. Yang, X. Huang, L. Chen, H. Li, *Nat. Energy* 4 (2019) 594–603.
- [30] J. Zheng, M.H. Engelhard, D. Mei, S. Jiao, B.J. Polzin, J.-G. Zhang, W. Xu, *Nat. Energy* 2 (2017) 17012.
- [31] T. Jin, Y. Wang, Z. Hui, B. Qie, A. Li, D. Paley, B. Xu, X. Wang, A. Chitu, H. Zhai, T. Gong, Y. Yang, *ACS Appl. Mater. Interfaces* 11 (2019) 17333–17340.
- [32] M. Ge, D.S. Coburn, E. Nazaretski, W. Xu, K. Gofron, H. Xu, Z. Yin, W.-K. Lee, *Appl. Phys. Lett.* 113 (2018), 083109.
- [33] G. Kresse, J. Furthmüller, *Phys. Rev. B* 54 (1996) 11169–11186.
- [34] G. Kresse, D. Joubert, *Phys. Rev. B* 59 (1999) 1758–1775.
- [35] J.P. Perdew, K. Burke, M. Ernzerhof, *Phys. Rev. Lett.* 77 (1996) 3865–3868.
- [36] F. Zhou, M. Cococcioni, C.A. Marianetti, D. Morgan, G. Ceder, *Phys. Rev. B* 70 (2004) 235121.
- [37] H.J. Monkhorst, J.D. Pack, *Phys. Rev. B* 13 (1976) 5188–5192.
- [38] D.R. Gallus, R. Schmitz, R. Wagner, B. Hoffmann, S. Nowak, I. Kekic-Laskovic, R.W. Schmitz, M. Winter, *Electrochim. Acta* 134 (2014) 393–398.
- [39] Z. Xu, M.M. Rahman, L. Mu, Y. Liu, F. Lin, *J. Mater. Chem.* 6 (2018) 21859–21884.
- [40] J. Becking, A. Gröbmeyer, M. Kolek, U. Rodehorst, S. Schulze, M. Winter, P. Bieker, M.C. Stan, *Adv. Mater. Interfaces* 4 (2017) 1700166.
- [41] J. Zheng, M. Gu, H. Chen, P. Meduri, M.H. Engelhard, J.-G. Zhang, J. Liu, J. Xiao, *J. Mater. Chem.* 1 (2013) 8464–8470.
- [42] G. Ceder, Y.M. Chiang, D.R. Sadoway, M.K. Aydinol, Y.I. Jang, B. Huang, *Nature* 392 (1998) 694–696.
- [43] M. Xie, T. Hu, L. Yang, Y. Zhou, *RSC Adv.* 6 (2016) 63250–63255.